PAPER

FeCoNiMnMo high-entropy alloy/carbon microspheres constructed *via* MOF-derived spray-drying granulation for enhanced oxygen evolution reaction

Tong Wu,[a] Ziyu Yang,[a] Zhilin Chen,[a] Rui Wang,[b] Ch. Venkata Reddy,[c] Jaesool Shim*[c] and Hui Tang [iD] *[a]

The development of efficient and durable oxygen evolution reaction (OER) electrocatalysts based on non-precious metals is crucial for advancing water-splitting technologies. Herein, we report a rational design and synthesis of FeCoNiMnMo high-entropy alloy(HEA) nanoparticles within hierarchical porous carbon microspheres (denoted as FeCoNiMnMo/C-MS) *via* a metal–organic framework (MOF)-derived spray-drying strategy. This method ensures atomic-level homogeneity of the metal precursors and constructs a unique microsphere architecture. Comprehensive characterization confirms the formation of a single-phase face-centered cubic (FCC) HEA with uniformly distributed elements. When evaluated as an OER catalyst, the FeCoNiMnMo/C-MS exhibits exceptional performance in alkaline media, requiring low overpotentials of only 380 and 406 mV to achieve current densities of 500 and 1000 mA cm^{-2}, respectively. It also demonstrates outstanding long-term stability, maintaining operation for over 400 hours at 400 mA cm^{-2}. The superior performance is attributed to the synergistic combination of the multi-element HEA core, which provides high intrinsic activity, and the porous carbon microsphere host, which facilitates mass transport and ensures structural robustness. This work presents a scalable synthesis route for high-performance non-precious OER catalysts.

Introduction

The escalating global energy demand, coupled with the urgent need to mitigate climate change, underscores a critical transition towards sustainable energy systems. In this context, hydrogen produced from renewable sources stands out as an ideal energy carrier due to its high energy density and zero carbon emissions.[1–3] Electrochemical water splitting, which converts intermittent renewable electricity into storable hydrogen, is a cornerstone technology for realizing this green hydrogen economy.[4–6] Nevertheless, the widespread adoption of this technology is hampered by the inefficiency of the anodic oxygen evolution reaction (OER)—a complex multi-step process involving four-electron transfers that inherently suffers from sluggish kinetics and high overpotential,[7–9] constituting the primary bottleneck for enhancing overall

energy conversion efficiency. Consequently, the development of high-performance OER electrocatalysts that integrate exceptional activity with long-term durability is imperative to reduce the energy input and improve the economic feasibility of water electrolysis.[10–12]

Recent years have witnessed the rise of high-entropy alloys (HEAs) as a promising class of electrocatalysts.[13–15] These materials, composed of multiple principal elements in near-equimolar ratios, exhibit unique properties such as high-entropy stabilization, severe lattice distortion, and the synergistic cocktail effect.[16–18] These characteristics collectively enable the fine-tuning of their electronic structures, which can optimize the binding energies of OER intermediates and enhance stability in oxidizing environments.[19–23] Currently, state-of-the-art OER catalysts often rely on Ir- or Ru-based HEAs,[24–26] which demonstrate commendable activity at low overpotentials. However, the prohibitive cost and natural scarcity of these noble metals pose significant barriers to their large-scale implementation. Furthermore, conventional methods for synthesizing HEAs (*e.g.*, arc melting and sputtering) are typically energy-intensive, and offer limited precision in controlling nano-structural features, thereby impeding the tailored design of

a School of Materials and Energy, University of Electronic Science and Technology of China, Chengdu, 611731, China. E-mail: tanghui@uestc.edu.cn
b School of Mechanical and Electrical Engineering, Chengdu University of Technology, Chengdu, 610059, China
c School of Mechanical Engineering, Yeungnam University, Gyeongsan 38541, Republic of Korea. E-mail: jshim@ynu.ac.kr

© 2026 The Author(s). Published by the Royal Society of Chemistry

RSC Appl. Interfaces, 2026, **3**, 475–484 | 475

high-performance catalysts.[27–29] In response, research efforts have pivoted towards designing HEAs composed exclusively of non-precious transition metals.[30,31] While this approach addresses the cost issue, achieving a combination of high activity, robust durability particularly at industrial-scale current densities and precise structural control remains a formidable challenge. Many reported non-noble HEAs still fall short in one or more of these aspects. Moreover, prevalent synthesis strategies often struggle to simultaneously ensure atomic-level homogeneity of multiple elements and construct desirable microarchitectures that facilitate mass and charge transport. Therefore, devising a scalable and controllable synthesis route to fabricate non-noble HEAs that excel in both intrinsic activity and structural efficacy is a crucial problem in the field.

Herein, we present a strategic design of a hierarchical porous HEA/C composite OER catalyst, scheme of the synthesis strategy is shown in Fig. 1, comprising Fe, Co, Ni, Mn, and Mo. Our methodology employs a metal–organic framework (MOF) precursor to achieve atomic-level dispersion and homogeneous mixing of the metal species. This is followed by a spray-drying process to engineer microspherical secondary structures, which are critical for enhancing mass transport and accessibility to active sites. Subsequent controlled thermal annealing in a reductive atmosphere facilitates the *in situ* formation of HEA nanoparticles within a conductive carbon matrix. The resulting FeCoNiMnMo HEA/C composite exhibits outstanding OER performance in alkaline media, characterized by low overpotentials at high current densities and exceptional long-term stability, demonstrating its potential for industrial application. This work not only

provides a catalyst with compelling performance but also establishes a versatile and scalable synthetic paradigm for the rational design of multi-elemental electrocatalysts, paving a new avenue for practical water-splitting technologies.

Experimental section

Materials

Iron(III) acetylacetonate ($C_{15}H_{21}FeO_6$, 98%), cobalt(III) acetylacetonate ($C_{15}H_{24}CoO_6$, 99%), nickel(II) acetylacetonate ($C_{10}H_{14}NiO_4$, 98%), cupric acetate ($C_4H_6CuO_4$, 99%), manganous acetate tetrahydrate ($C_4H_6MnO_4 \cdot 4H_2O$, 99%), bis(acetylacetonato)dioxomolybdenum(VI) ($C_{10}H_{14}MoO_6$, 97%), 2,5-dihydroxyterephthalic acid (2,5-BDC, 99%), potassium hydroxide (KOH, 99%), polyvinyl pyrrolidone (PVP, 99%), N,N-dimethylformamide (DMF, 99.9%), ethanol (99%), Nafion solution (5 wt%) and ruthenium oxide (RuO_2, 99%) were purchased from Adamas-beta Co., LTD (Shanghai, China). Nickel foam (NF) were purchased from Suzhou Zhengrong New Material Co., LTD. All the chemical reagents were used directly without further purification. Ultrapure water from a laboratory water purification system (XUC-40) (resistivity 18.5 MΩ cm) was used to prepare all aqueous electrolyte solutions.

Synthesis of FeCoNiMnMo-MOF precursor

The FeCoNiCuMnMo multi-metallic MOFs were synthesized *via* one step solvothermal method.[32] Briefly, 2.4 mmol total of the metal precursors—$C_{15}H_{21}FeO_6$, $C_2H_4CoO_2$, $C_{10}H_{14}NiO_4$, $C_4H_6MnO_4 \cdot 4H_2O$, and $C_{10}H_{14}MoO_6$—were co-dissolved in a mixed solution of 70 mL of DMF, 5 ml ethanol and 5 ml ultrapure water to form a homogeneous precursor solution.
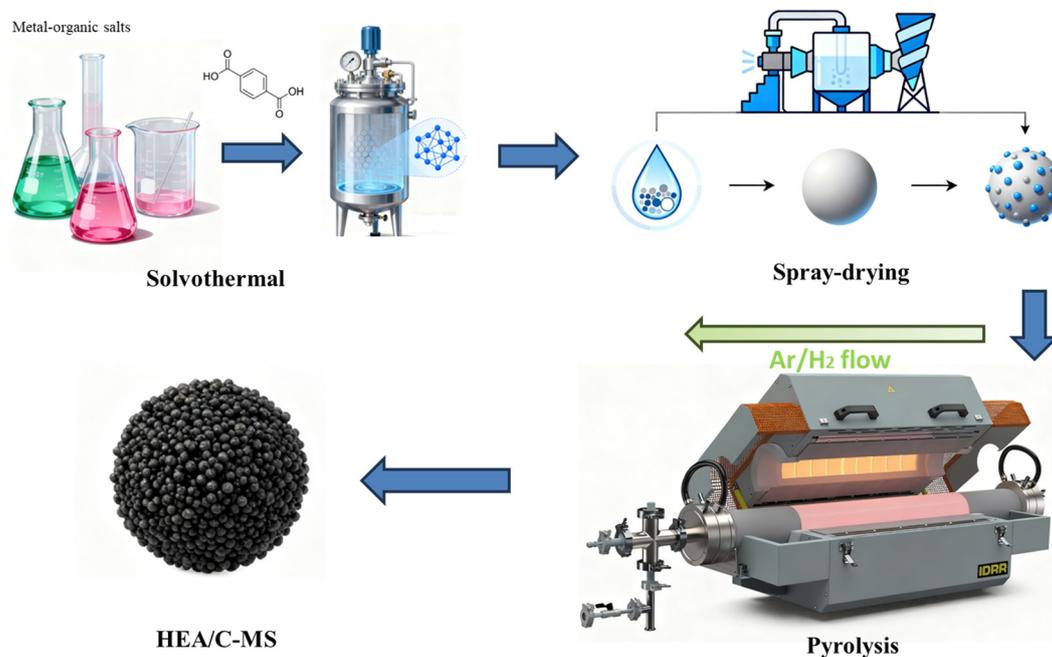

Fig. 1 Schematic illustration of the catalyst preparation procedures.

Subsequently, three times the molar amount s of 2,5-BDC (7.2 mmol) was introduced as the organic linker. The mixed solution was stirred under continuous magnetic agitation for 30 minutes to make sure complete dissolution. After that, the homogenous solution was transferred into pressure reactor, the solvothermal reaction was under 120 °C, lasting for 24 h. The resulting solid products were collected by centrifugation, purified *via* repeated washing with ethanol and de-ion water for three times, and finally vacuum-dried at 60 °C overnight. The obtained samples were accordingly denoted as FeCoNiCuMnMo-MOF.

Synthesis of FeCoNiMnMo/C catalyst

The FeCoNiMnMo-MOF precursor was pre-decomposed in a tube furnace at 350 °C for 1 h first, and then annealed at 700 °C for 2 h, both steps were under Ar/H$_2$ atmosphere (H$_2$ 5%, Ar 95%). After cooling to room temperature, the obtained samples were ground with an agate mortar. The final samples were accordingly noted as FeCoNiMnMo/C.

Synthesis of FeCoNiMnMo/C-MS catalyst

The FeCoNiMnMo-MOF was dispersed in ultrapure water to obtain a turbid solution of 10 mg ml^{-1}, and then 1 wt% PVP was added as a surfactant to obtain a relatively stable suspension. The suspension was sprayed out at a speed of 50 ml per hour at 280 °C in a spray dryer for secondary granulation, and the powder obtained through spray drying was pre-decomposed in a tube furnace at 350 °C for 1 h first, and then annealed at 700 °C for 2 h, both steps were under Ar/H$_2$ atmosphere (H$_2$ 5%, Ar 95%,). After cooling to room temperature, the obtained samples were ground with an agate mortar. The final samples were accordingly noted as FeCoNiMnMo/C-MS.

Synthesis of comparative samples

For comparison, FeCoNiMo/Cand FeCoNiMnCu/C were synthesized following an identical procedure to the FeCoNiMnMo/C. FeCoNiMnCu/C-MS was synthesized following an identical procedure to the FeCoNiMnMo/C-MS.

Synthesis of catalyst/NF working electrode

A catalyst ink was prepared by dispersing 10 mg of the catalyst powder in 1 mL of a Nafion/ethanol solution (prepared from 950 μL ethanol and 50 μL of 5 wt% Nafion) and ultrasonic dispersion for 1 hour.[33] The ultrasonic dispersion process is carried out in ice bath entirely. Subsequently, 100 μL of the homogeneous ink was cast onto a 5 × 5 mm NF substrate and dried under ambient conditions to obtain catalyst/NF as work electrode for electrochemical test. All of those ink samples were prepared under the same procedure.

Materials characterization

The microstructural morphology and elemental composition of the synthesized samples were examined using a field emission scanning electron microscope (FE-SEM, FEI Sirion) equipped with an energy-dispersive X-ray spectroscopy (EDS) detector, operating at an acceleration voltage of 20 kV. Further nanoscale structural analysis was performed *via* high-resolution transmission electron microscopy (HRTEM) on an FEI Tecnai G2 instrument. The crystalline phases were identified by X-ray diffraction (XRD) on a DX-2700BH diffractometer using Cu Kα radiation (λ = 1.5418 Å) under operating conditions of 40 kV and 35 mA. Surface chemical states were probed by X-ray photoelectron spectroscopy (XPS) on a Kratos Axis Ultra spectrometer with an Al Kα X-ray source. All XPS binding energies were calibrated with reference to the adventitious carbon C 1s peak set at 284.6 eV.

Electrochemical measurements

The electrocatalytic performance was evaluated using a standard three-electrode configuration connected to a CHI 660E electrochemical workstation (Chenhua, Shanghai, China), with all measurements conducted at ambient temperature (25 ± 3 °C). A catalyst-loaded nickel foam (catalyst/NF) served as the working electrode, while a Hg/HgO electrode (calibrated to +0.926 V *vs.* RHE in 1 M KOH at 25 °C) and a carbon rod were employed as the reference and counter electrodes, respectively. Prior to data collection, the working electrode was activated by performing 30 cyclic voltammetry (CV) cycles between 1.2 V and 1.9 V (*vs.* RHE) at a scan rate of 50 mV s^{-1}. Linear sweep voltammetry (LSV) and corresponding Tafel plots were then acquired in 1 M KOH at a scan rate of 5 mV s^{-1}. Electrochemical impedance spectroscopy (EIS) was carried out across a frequency range of 0.1 to 100 kHz, applied at overpotentials of 200, 250, 300, and 350 mV. The electrochemically active surface area (ECSA) was determined from CVs measured in a non-Faradaic potential window at scan rates ranging from 20 to 120 mV s^{-1}. The double-layer capacitance (C_{dl}) was derived from the slope of the charging current *versus* scan rate plot, and the ECSA was subsequently calculated using the formula ECSA = C_{dl}/C_s, where a standard specific capacitance (C_s) value of 40 μF cm^{-2} was applied.

Results and discussion

Morphology, phase, and structure analysis of catalysts

The crystalline structure and microscopic morphology of the as-prepared material were unequivocally determined by XRD, SEM and TEM. The collective evidence confirms the successful synthesis of HEA/C-MS, in which HEA nanoparticles are embedded within a carbon matrix (denoted as FeCoNiMnMo/C-MS), *via* a synthetic route involving MOF-derived precursors and subsequent spray-drying. The XRD pattern (Fig. 2a) exhibits characteristic peaks of a face-
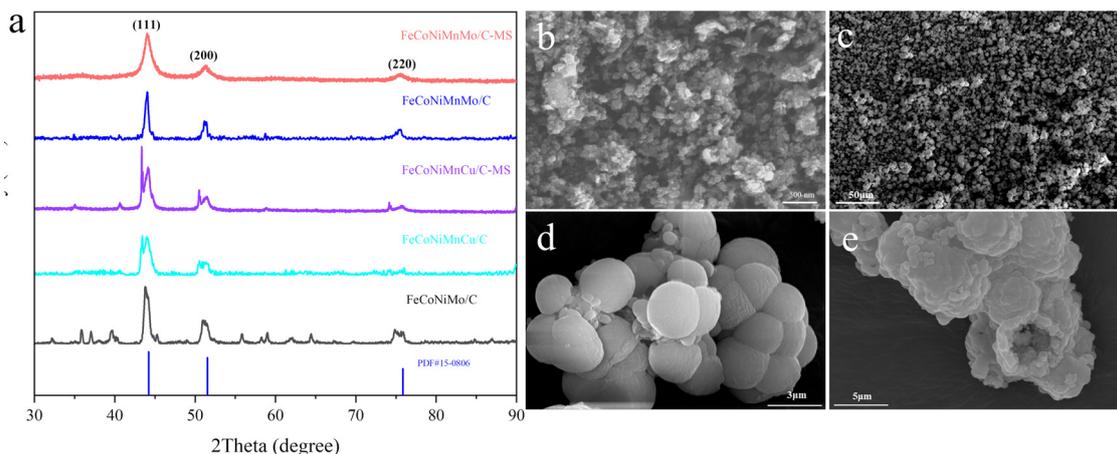
© 2026 The Author(s). Published by the Royal Society of Chemistry

RSC Appl. Interfaces, 2026, **3**, 475–484 | **477**

Fig. 2 a. XRD patterns of FeCoNiMnMo/C-MS, FeCoNiMnCu/C-MS, FeCoNiMnMo/C, FeCoNiMnCu/C and FeCoNiMo/C. b. SEM image of the FeCoNiMnMo/C. (c–e) SEM images of the FeCoNiMnMo/C-MS microspheres obtained *via* the spray-drying strategy.

centered cubic (FCC) crystal structure of FeCoNiMnMo/C-MS, which are unambiguously indexed to the (111), (200), and (220) lattice planes. Crucially, the absence of any extraneous diffraction peaks attributable to individual metals or their oxides provides definitive evidence for the formation of a single-phase solid solution alloy comprising Fe, Co, Ni, Mn, and Mo under the applied synthesis conditions. SEM images (Fig. 2b–e) reveal a well-defined architecture of three-dimensional, hierarchical porous microspheres with diameters on the order of 2–5 micrometers. Fig. 2b indicates that the samples directly annealed in a reducing atmosphere without spray drying are small particles at the nanoscale. Fig. 2c–e shows that the sample obtained after spray-drying secondary granulation followed by annealing is a hollow microsphere composed of smaller particles. This distinctive

morphology is a direct consequence of the employed synthesis strategy: the initial spray-drying process constructs the spherical macro-framework, while the subsequent pyrolysis preserves, to a significant extent, the innate porosity of the MOF precursor. Concurrently, the carbonization of organic linkers and the reduction/alloying of metal nodes collaboratively finalize this hierarchical porous architecture. The microscopic structure and elemental distribution of the representative FeCoNiMnMo/C-MS catalyst were further elucidated through TEM and associated techniques.

As shown in Fig. 3a, the low-magnification TEM image confirms the microspherical architecture, which is constructed from numerous densely packed nanoparticles. This observation is in excellent agreement with the SEM results, solidifying the hierarchical nature of the material. To
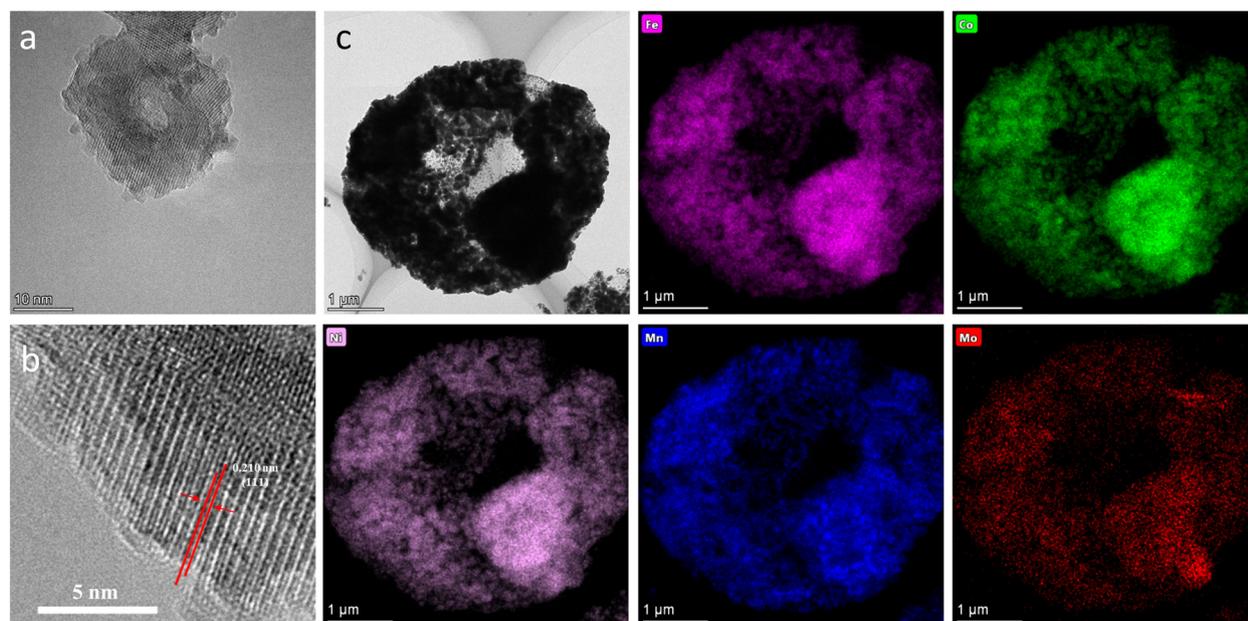

Fig. 3 a. TEM image of FeCoNiMnMo/C b. HRTEM image of FeCoNiMnMo/C-MS c. TEM and EDS mapping of FeCoNiMnMo/C-MS.
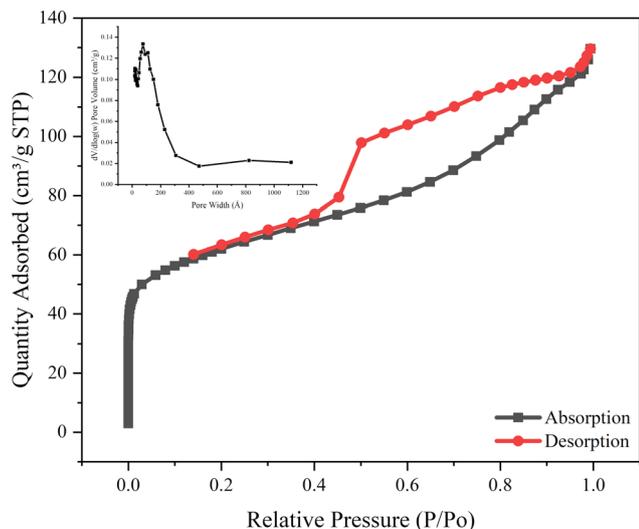
Fig. 4 Isotherm linear plot and BJH adsorption $dV/d\log(w)$ pore volume of FeCoNiMnMo/C-MS.

gain deeper crystallographic insights, HRTEM analysis was conducted. A representative HRTEM image (Fig. 3b) reveals well-defined lattice fringes with an interplanar spacing measured to be 2.10 Å. This value can be confidently indexed to the (111) crystallographic plane of a FCC structure.[34,35] Notably, this measured d-spacing exhibits an excellent correspondence with the d-value of 2.06 Å calculated from the (111) diffraction peak ($2\theta = 44.04°$) in the XRD pattern. The minor discrepancy is within the typical margin of error for the respective techniques. This perfect mutual validation

between HRTEM and XRD confirms the high crystallinity of the material and provides definitive proof that the nanoparticles supported on the carbon matrix are the intended single-phase FCC HEA solid solution. Crucially, EDS elemental mapping was performed to probe the spatial distribution of the constituent elements. As presented in Fig. 3c, the signals for Fe, Co, Ni, Mn, Mo, and C homogeneously distributed at the micrometer scale with minor nanoscale fluctuations This homogeneous dispersion of all five metallic elements at the nanoscale provides direct and compelling evidence for the successful formation of a high-entropy alloy, consistent with the single-phase solid solution structure identified by XRD. The pore structure of the material was systematically analyzed by the nitrogen physical adsorption method. The specific surface area of the material was calculated using the BET method, which was 208.8 m^2 g^{-1}, and the total pore volume was 0.200 cm^3 g^{-1}. As shown in Fig. 4, the nitrogen adsorption–desorption isotherm exhibited typical IV-type characteristics, and a clear H2-type hysteresis loop was observed within the P/P_0 range of 0.40–0.90. This confirmed the presence of a multi-level pore structure dominated by mesopores in the material.

Surface chemical state analysis

As shown in Fig. 5(a–f), the surface chemical states and elemental composition of the as-synthesized FeCoNiMnMo/C-MS probed by XPS. The spectra confirmed the co-existence of all five constituent metallic elements (Fe, Co, Ni, Mn, Mo) along with the carbon matrix. Deconvolution of the individual spectra revealed the dominant oxidized nature of
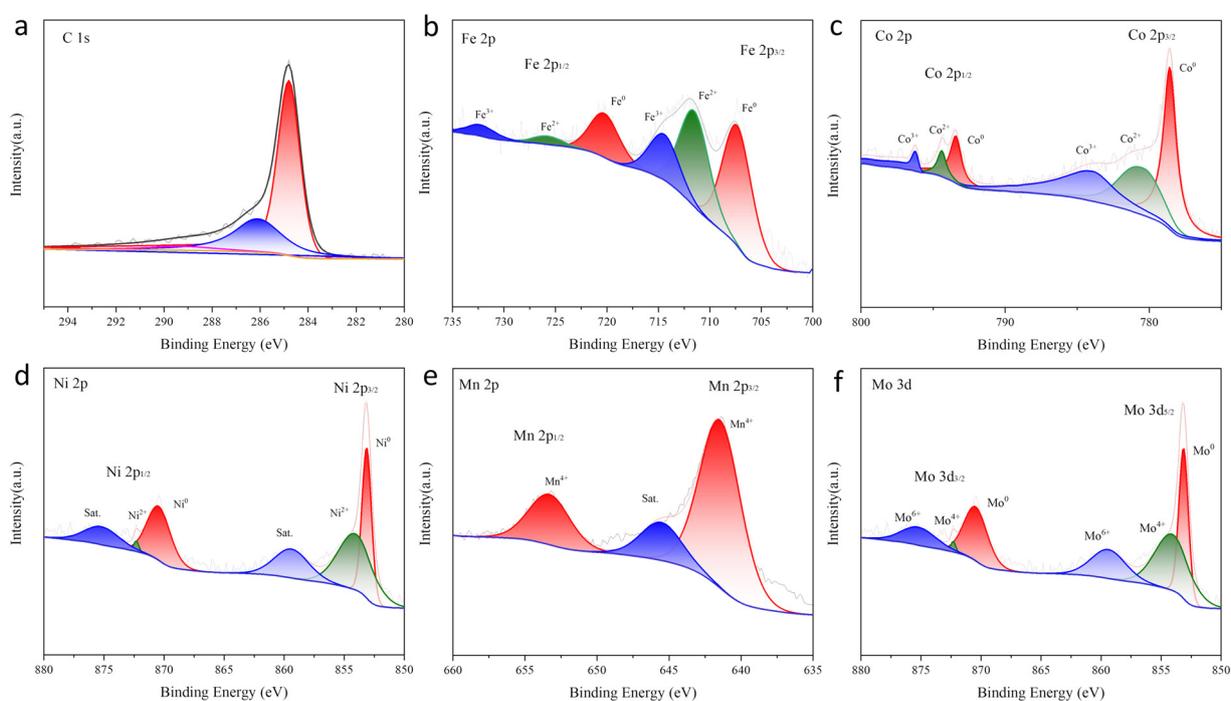

Fig. 5 XPS spectrum of FeCoNiMnMo/C-MS (a–f) C1s, Fe2p, Co2p, Ni2p, Mn2p and Mo3d respectively.

© 2026 The Author(s). Published by the Royal Society of Chemistry

RSC Appl. Interfaces, 2026, **3**, 475–484 | **479**

the metal species on the surface. In the Fe 2p spectrum (Fig. 5b), the Fe $2p_{3/2}$ region is fitted with components at approximately 707.0 eV, 711.5 eV, and 714.5 eV, corresponding to Fe^0, Fe^{2+}, and Fe^{3+}, respectively, accompanied by a satellite peak near 718 eV. Similarly, the Co 2p spectrum (Fig. 5c) shows peaks for Co^0 (~778.0 eV), Co^{2+} (~781.0 eV), and Co^{3+} (~783.0 eV) in the Co $2p_{3/2}$ region, along with its associated satellite feature. The Ni 2p spectrum (Fig. 5d) also displays a mixed valence state, with Ni^0 (~852.0 eV), Ni^{2+} (~855.0 eV), contributions in the Ni $2p_{3/2}$ envelope. Notably, the Mn 2p spectrum (Fig. 5e) is dominated by a peak at ~641.0 (Mn $2p_{3/2}$), characteristic of the Mn^{4+} oxidation state. Meanwhile, the Mo 3d spectrum (Fig. 5f) is predominated by the Mo^{6+} state (Mo $3d_{5/2}$ at ~858.5 eV), with a minor contribution from Mo^{4+} (~853.0 eV), while the signal for metallic Mo^0 is also exsit. Complementing these findings, the C 1s spectrum (Fig. 5a) could be deconvoluted into a primary component at 284.8 eV, attributed to graphitic sp^2 carbon, and higher-binding-energy components corresponding to carbon–oxygen functional groups. These XPS results collectively verify the successful formation of the HEA/C composite and highlight the presence of a complex surface oxide layer, which is anticipated to serve as a pre-

catalyst for efficient electrochemical reactions such as the OER.[36,37]

Electrocatalytic OER performance

A comprehensive evaluation of the OER performance for all synthesized catalysts and reference materials was conducted, with key metrics for direct comparison. The intrinsic catalytic activity was first evaluated by linear sweep voltammetry, with the overpotential at 500 and 1000 mA cm^{-2} serving as the key metric for industrial relevance. As shown in Fig. 6a, the FeCoNiMnMo/C-MS catalyst demonstrated superior activity, requiring the lowest overpotentials of only 380 mV and 406 mV, respectively. The FeCoNiMnCu/C-MS sample followed closely, with overpotentials of 392 mV and 425 mV. In contrast, the counterparts without the microsphere structure, FeCoNiMnMo/C and FeCoNiMnCu/C, as shown in Fig. 6c, exhibited significantly higher overpotentials (e.g., 405 mV and 444 mV for Mo-based; 413 mV and 458 mV for Cu-based), highlighting the critical role of the porous microsphere architecture in enhancing performance at high current densities. Both multimetal catalysts substantially outperformed the commercial benchmark RuO_2 (491 mV @
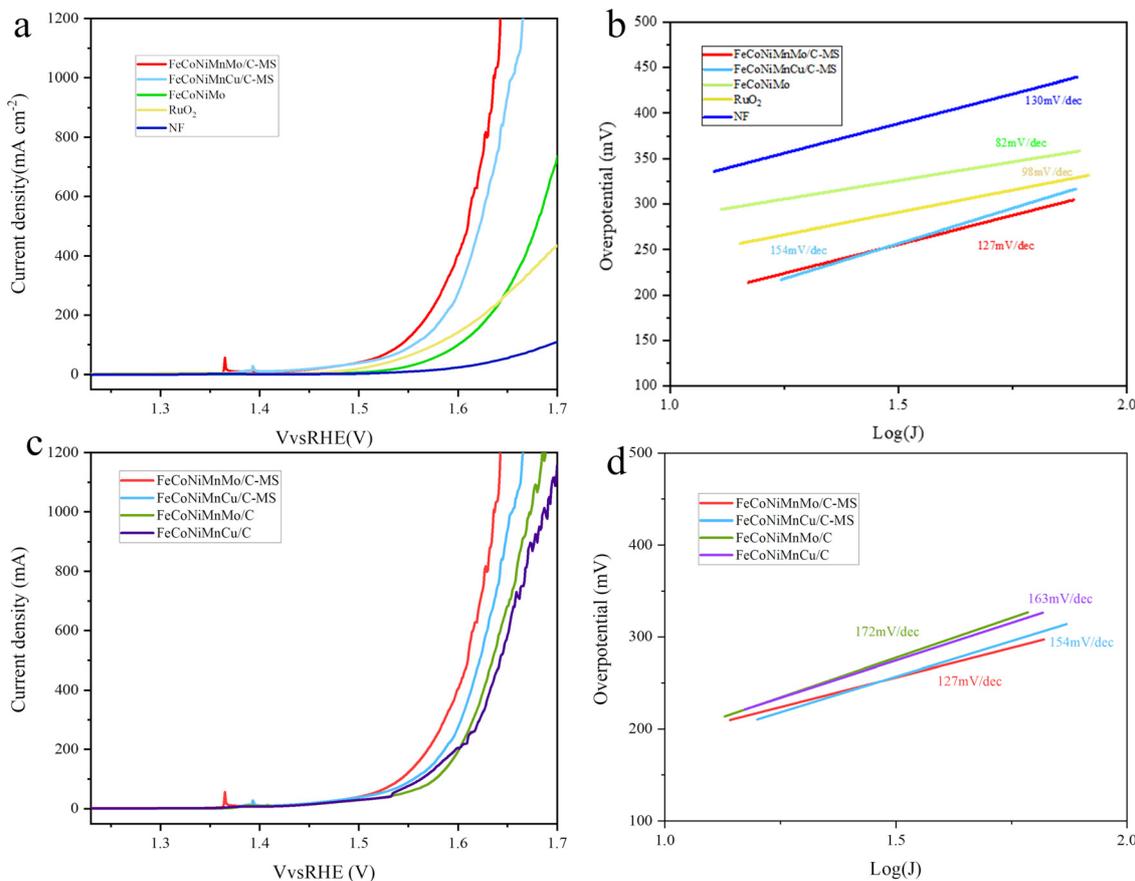

Fig. 6 Electrocatalytic performance of FeCoNiMnMo/C-MS a and b LSV and Tafel slope of FeCoNiMnMo/C-MS, FeCoNiMnCu/C-MS, FeCoNiMnMo/C, RuO_2 and NF. c and d LSV and Tafel slope of FeCoNiMnMo/C-MS, FeCoNiMnCu/C-MS, FeCoNiMnMo/C and FeCoNiMnCu/C.
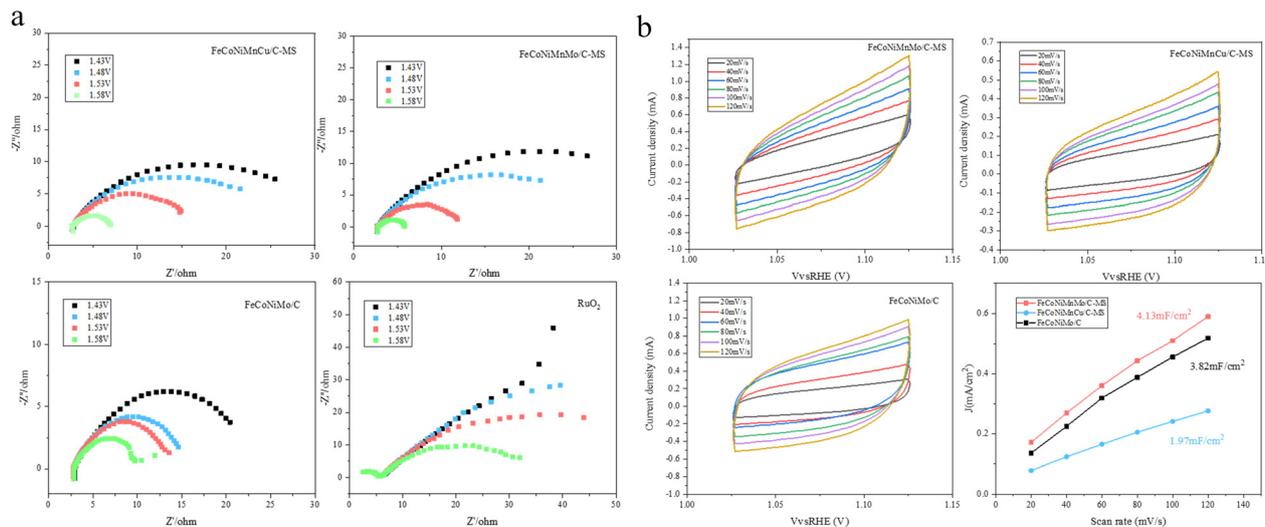
480 | RSC Appl. Interfaces, 2026, **3**, 475–484

© 2026 The Author(s). Published by the Royal Society of Chemistry

Fig. 7 a. EIS curves of FeCoNiMnMo/C-MS FeCoNiMnCu/C FeCoNiMnMo/C RuO$_2$ at different voltage. b. CV curves and Cdls of FeCoNiMnMo/C-MS FeCoNiMnCu/C FeCoNiMnMo/C.

500 mA cm^{-2}) and the bare NF substrate. The reaction kinetics were investigated through Tafel analysis and electrochemical impedance spectroscopy (EIS). Notably, as demonstrate in Fig. 6b and d the Tafel slopes for both MS-

structured catalysts were significantly lower than their non-MS counterparts (FeCoNiMnMo/C: 172 mV dec^{-1}; FeCoNiMnCu/C: 163 mV dec^{-1}), and also superior to that of NF (130 mV dec^{-1}). While the commercial RuO$_2$ exhibited
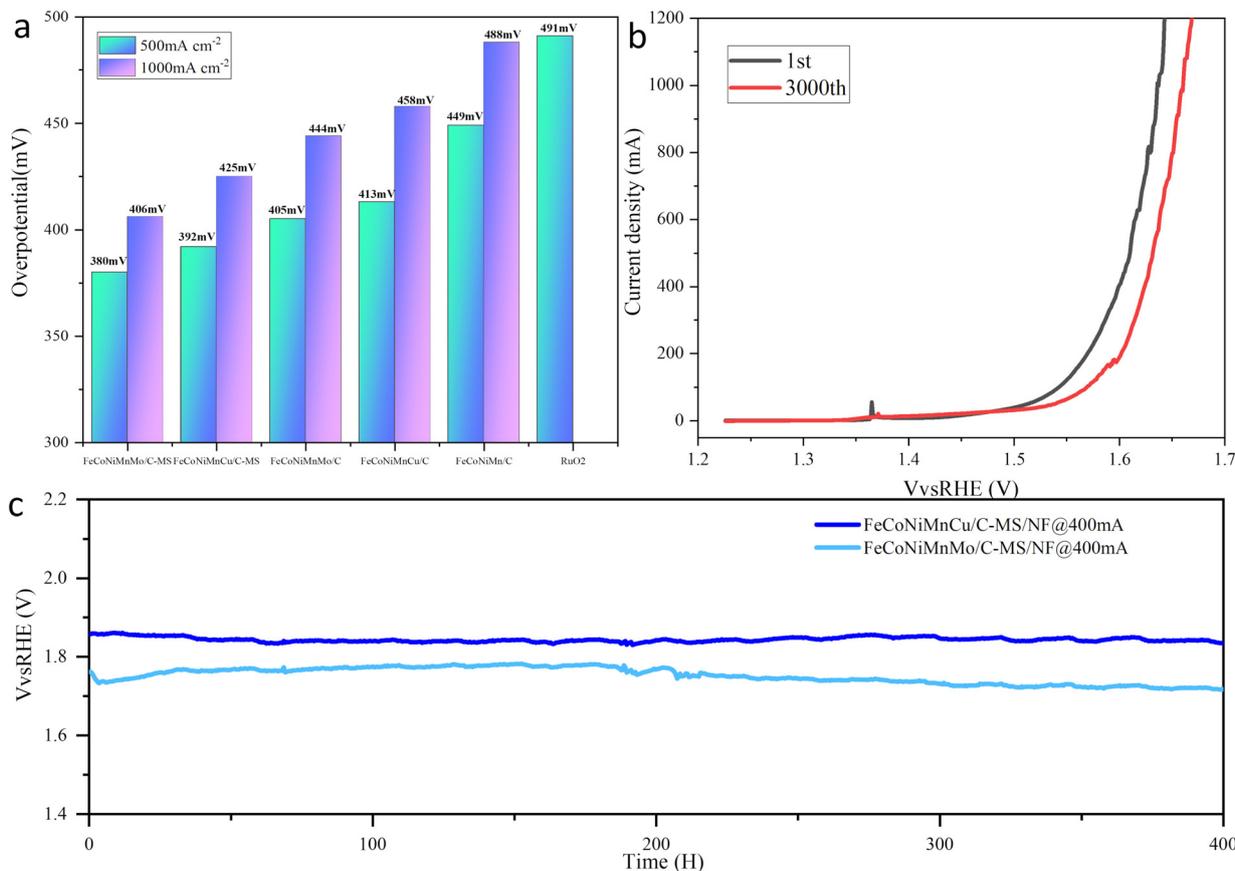

Fig. 8 a. the overpotential comparison of different catalysts at current density of 500 mA cm^{-2} and 1 A cm^{-2} b. LSV curves of FeCoNiMnMo/C-MS for first run and after 3000 cycles. c. Long term stability of FeCoNiMnMo/C-MS and FeCoNiMnCu/C-MS at 400 mA cm^{-2}.

© 2026 The Author(s). Published by the Royal Society of Chemistry

RSC Appl. Interfaces, 2026, **3**, 475–484 | 481

the lowest Tafel slope (98 mV dec^{-1}) among all samples, however, its overall performance, particularly at high current densities and during long-term operation, is limited by factors such as a lower electrochemically active surface area and potential instability.

This kinetic advantage of the multimetal catalysts is further corroborated by EIS results, Fig. 7a showed that FeCoNiMnMo/C-MS possessed the smallest charge-transfer resistance (R_{ct}), followed by FeCoNiMnCu/C-MS, confirming the most efficient charge transfer at the electrode–electrolyte interface. The density of accessible active sites was probed by measuring the double-layer capacitance (C_{dl}). As demonstrate in Fig. 7b, the FeCoNiMnMo/C-MS catalyst yielded the largest C_{dl} value (4.13 mF), indicating it possesses the most abundant electrochemically active surface area, which can be directly attributed to its hierarchical porous microsphere morphology as revealed by SEM and TEM. The FeCoNiMnCu/C-MS sample ranked third (1.97 mF), and FeCoNiMnMo/C-MS catalyst exhibiting significantly higher C_{dl} than its non-MS counterparts FeCoNiMnMo/C (3.82 mF). This result directly links the hierarchical porous microstructure of the MS series to the exposure of a greater number of active sites, which is a fundamental contributor to their enhanced catalytic activity.

Fig. 8a visually compares the overpotential indicators of each catalyst. Our comprehensive electrochemical evaluation reveals that the FeCoNiMnMo/C-MS catalyst could become a highly promising candidate, surpassing commercial RuO$_2$ and a suite of synthesized counterparts, establishing a clear performance hierarchy: FeCoNiMnMo/C-MS > FeCoNiMnCu/C-MS > FeCoNiMnMo. The superior performance of the Mo-containing catalyst over its Cu-containing counterpart suggests that the incorporation of Mo^{6+}, as identified by XPS, more effectively modulates the electronic structure of the active sites, potentially optimizing the adsorption energy of oxygen intermediates. Moreover, both FeCoNiMnMo/C-MS and FeCoNiMnCu/C-MS exhibited exceptional durability. As shown in Fig. 8b, after 3000 continuous CV cycles, the FeCoNiMnMo/C-MS LSV curve showed an activity loss caused by the spalling of the catalyst, which is acceptable for particle catalysts. More importantly, in chronopotentiometry tests conducted at a constant high current density of 400 mA cm^{-2} (Fig. 8c), both catalysts maintained a stable potential over 400 hours, demonstrating remarkable structural and compositional robustness. According to relevant studies,[38,39] in the FeCoNiMnMo heterogeneous alloy, the strong high-entropy effect significantly inhibits the dissolution of all elements (especially the soluble Mo and Mn), and causes the growth of the surface-reconstructed (hydroxyl) hydroxide catalytic layer to be extremely slow; meanwhile, the electronic structure regulated by Mo (optimized d-band center, appropriate intermediate adsorption energy, the electron transfer by Mo causing a moderate downward shift of the d-band center of Fe/Co/Ni, and weakening the overly strong adsorption of oxygen-containing intermediates such as *OH,

*O) directly endows the alloy with inherent high OER activity.

Conclusion

In conclusion, we have successfully fabricated FeCoNiMnMo HEA/C-MS composites through an innovative MOF-derived spray-drying and annealing approach. The FeCoNiMnMo/C-MS catalyst emerges as a highly efficient and robust OER electrocatalyst, characterized by an optimal combination of low overpotential at industrial-level current densities, favorable reaction kinetics, and exceptional long-term durability. The key to its performance lies in the synergistic design: the multi-element HEA core provides a tailored electronic structure for optimizing intermediate adsorption, while the hierarchically porous carbon microsphere architecture ensures maximal exposure of active sites, efficient mass transport, and remarkable mechanical stability. The performance enhancement of the MS-series catalysts over their non-spherical counterparts underscores the improvement of macroscopic structural engineering in electrocatalysis. This work not only delivers a promising catalyst candidate for practical water electrolysis but also establishes a versatile and scalable synthetic paradigm for designing advanced multi-elemental materials for energy conversion and beyond.

Conflicts of interest

There are no conflicts to declare.

Data availability

All data presented in this manuscript can be provided by the corresponding author on reasonable demand.

XRD pattern, SEM and EDS mapping images, HRTEM image, LSV curves, and CV curves are available in supplementary information (SI). See DOI: https://doi.org/10.1039/d5lf00351b.

References

1 U. S. Behera, J. S. Sangwai and H.-S. Byun, A comprehensive review on the recent advances in applications of nanofluids for effective utilization of renewable energy, *Renewable Sustainable Energy Rev.*, 2025, **207**, 114901.

2 G. Yang, G. Zhang, D. Cao, D. Zha, X. Gao and B. Su, China's provincial-level sustainable energy transition requires accelerating renewable energy technological innovation, *Energy*, 2024, **288**, 129672.

3 L. Tang, H. Peng, J. Kang, H. Chen, M. Zhang, Y. Liu, D. H. Kim, Y. Liu and Z. Lin, Zn-based batteries for sustainable energy storage: strategies and mechanisms, *Chem. Soc. Rev.*, 2024, **53**, 4877–4925.

4 R. Guo and T. He, High-Entropy Perovskite Electrolyte for Protonic Ceramic Fuel Cells Operating below 600 °C, *ACS Mater. Lett.*, 2022, **4**, 1646–1652.

5 I. Hussain, C. Lamiel, M. Ahmad, Y. Chen, S. Shuang, M. S. Javed, Y. Yang and K. Zhang, High entropy alloys as electrode material for supercapacitors: A review, *J. Energy Storage*, 2021, **44**, 103405.

6 Y. Chen, H. Fu, Y. Huang, L. Huang, X. Zheng, Y. Dai, Y. Huang and W. Luo, Opportunities for High-Entropy Materials in Rechargeable Batteries, *ACS Mater. Lett.*, 2021, **3**, 160–170.

7 X. F. Lu, B. Y. Xia, S. Zang and X. W. (David) Lou, Metal–Organic Frameworks Based Electrocatalysts for the Oxygen Reduction Reaction, *Angew. Chem., Int. Ed.*, 2020, **132**, 4662–4678.

8 J. Zhang, H. Yang and B. Liu, Coordination Engineering of Single-Atom Catalysts for the Oxygen Reduction Reaction: A Review, *Adv. Energy Mater.*, 2021, **11**, 2002473.

9 Y. Zhao, D. P. A. Saseendran, C. Huang, C. A. Triana, W. R. Marks, H. Chen, H. Zhao and G. R. Patzke, Oxygen Evolution/Reduction Reaction Catalysts: From In Situ Monitoring and Reaction Mechanisms to Rational Design, *Chem. Rev.*, 2023, **123**, 6257–6358.

10 X. Tian, X. F. Lu, B. Y. Xia and X. W. (David) Lou, Advanced Electrocatalysts for the Oxygen Reduction Reaction in Energy Conversion Technologies, *Joule*, 2020, **4**, 45–68.

11 Z. Liang, H. Guo, G. Zhou, K. Guo, B. Wang, H. Lei, W. Zhang, H. Zheng, U. Apfel and R. Cao, Metal–Organic-Framework-Supported Molecular Electrocatalysis for the Oxygen Reduction Reaction, *Angew. Chem., Int. Ed.*, 2021, **133**, 8553–8557.

12 M. A. Ud Din, M. Idrees, S. Jamil, S. Irfan, G. Nazir, M. A. Mudassir, M. S. Saleem, S. Batool, N. Cheng and R. Saidur, Advances and challenges of methanol-tolerant oxygen reduction reaction electrocatalysts for the direct methanol fuel cell, *J. Energy Chem.*, 2023, **77**, 499–513.

13 E. P. George, D. Raabe and R. O. Ritchie, High-entropy alloys, *Nat. Rev. Mater.*, 2019, **4**, 515–534.

14 J.-T. Ren, L. Chen, H.-Y. Wang and Z.-Y. Yuan, High-entropy alloys in electrocatalysis: from fundamentals to applications, *Chem. Soc. Rev.*, 2023, **52**, 8319–8373.

15 X. Chang, M. Zeng, K. Liu and L. Fu, Phase Engineering of High-Entropy Alloys, *Adv. Mater.*, 2020, **32**, 1907226.

16 E. P. George, W. A. Curtin and C. C. Tasan, High entropy alloys: A focused review of mechanical properties and deformation mechanisms, *Acta Mater.*, 2020, **188**, 435–474.

17 X. Yan, Functional properties and promising applications of high entropy alloys, *Scr. Mater.*, 2020, **187**, 188–193.

18 C. Oses, C. Toher and S. Curtarolo, High-entropy ceramics, *Nat. Rev. Mater.*, 2020, **5**, 295–309.

19 X. Lincheng, W. Yue, Y. Yong, H. Zhanzhong, C. Xin and L. Fan, Triggering efficient Mn active centers by tuning the localized Sr^{2+} sites in high-entropy ABO_3 oxygen electrocatalysis, *Chem. Eng. J.*, 2024, **485**, 149755.

20 Y. Lao, X. Huang, L. Liu, X. Mo, J. Huang, Y. Qin, Q. Mo, X. Hui, Z. Yang and W. Jiang, Structure-activity relationship study of high entropy oxides catalysts for oxygen evolution reaction, *Chem. Eng. J.*, 2024, **481**, 148428.

21 H. Nan, S. Lv, Z. Xu, Y. Feng, Y. Zhou, M. Liu, T. Wang, X. Liu, X. Hu and H. Tian, Inducing the cocktail effect in yolk-shell high-entropy perovskite oxides using an electronic structural design for improved electrochemical applications, *Chem. Eng. J.*, 2023, **452**, 139501.

22 Z. Wang, High-entropy phosphate/C hybrid nanosheets for efficient acidic hydrogen evolution reaction, *Chem. Eng. J.*, 2022, **437**, 135375.

23 S. Liao, Engineering High-Entropy Duel-Functional nanocatalysts with regulative oxygen vacancies for efficient overall water splitting, *Chem. Eng. J.*, 2023, **471**, 144506.

24 J. Hao, Z. Zhuang, K. Cao, G. Gao, C. Wang, F. Lai, S. Lu, P. Ma, W. Dong, T. Liu, M. Du and H. Zhu, Unraveling the electronegativity-dominated intermediate adsorption on high-entropy alloy electrocatalysts, *Nat. Commun.*, 2022, **13**, 2662.

25 K. Miao, W. Jiang, Z. Chen, Y. Luo, D. Xiang, C. Wang and X. Kang, Hollow-Structured and Polyhedron-Shaped High Entropy Oxide toward Highly Active and Robust Oxygen Evolution Reaction in a Full pH Range, *Adv. Mater.*, 2024, **36**, 2308490.

26 Z. Jin, X. Zhou, Y. Hu, X. Tang, K. Hu, K. M. Reddy, X. Lin and H.-J. Qiu, A fourteen-component high-entropy alloy@oxide bifunctional electrocatalyst with a record-low Δ E of 0.61 V for highly reversible Zn–air batteries, *Chem. Sci.*, 2022, **13**, 12056–12064.

27 A. H. Karabacak, A. Çanakçı, S. Özkaya, S. A. Tunç, O. Güler and M. Çelebi, Effect of AlCrCuFeNi high entropy alloy reinforcements with and without B_4C on powder characteristic, mechanical and wear properties of AA5083 metal-metal composites, *J. Alloys Compd.*, 2024, **1008**, 176627.

28 C. Gao, Y. Zhang, D. Li, P. Wu and C. Shuai, Mechanical alloying and laser powder bed fusion: A potential preparation route for homogenized equiatomic TiTaNbZr high-entropy alloys with excellent wear and corrosion resistances, *J. Alloys Compd.*, 2025, **1036**, 182116.

29 M. He, H. Kang, G. Hou, Z. Lian, S. Lu, Y. Li, W. Qin and X. Wu, Fabrication of eutectic FeCrCoNiV1.5 high entropy alloy coating with excellent high-temperature wear resistance, *Surf. Coat. Technol.*, 2024, **476**, 130232.

30 Y. Cui, S. Jiang, Q. Fu, R. Wang, P. Xu, Y. Sui, X. Wang, Z. Ning, J. Sun, X. Sun, A. Nikiforov and B. Song, Cost-Effective High Entropy Core–Shell Fiber for Stable Oxygen Evolution Reaction at 2 A cm^{-2}, *Adv. Funct. Mater.*, 2023, **33**, 2306889.

31 H. Liu, H. Qin, J. Kang, L. Ma, G. Chen, Q. Huang, Z. Zhang, E. Liu, H. Lu, J. Li and N. Zhao, A freestanding nanoporous NiCoFeMoMn high-entropy alloy as an efficient electrocatalyst for rapid water splitting, *Chem. Eng. J.*, 2022, **435**, 134898.

32 S. Wang, W. Huo, F. Fang, Z. Xie, J. K. Shang and J. Jiang, High entropy alloy/C nanoparticles derived from polymetallic MOF as promising electrocatalysts for alkaline oxygen evolution reaction, *Chem. Eng. J.*, 2022, **429**, 132410.

33 X. Liu, S. Xi, H. Kim, A. Kumar, J. Lee, J. Wang, N. Q. Tran, T. Yang, X. Shao, M. Liang, M. G. Kim and H. Lee, Restructuring highly electron-deficient metal-metal oxides for boosting stability in acidic oxygen evolution reaction, *Nat. Commun.*, 2021, **12**, 5676.

© 2026 The Author(s). Published by the Royal Society of Chemistry

RSC Appl. Interfaces, 2026, **3**, 475–484 | **483**

34 J. Wang, W. Liu, Y. Wang, Y. Guo, M. Liu, C. Ye, S. Wang and Q. Zou, AgCuInCdZn high-entropy alloy nanoparticles-embedded in porous carbon fibers for long-cycling lithium metal anodes, *Chem. Eng. J.*, 2023, **477**, 146884.

35 H. Bian, P. Qi, G. Xie, X. Liu, Y. Zeng, D. Zhang and P. Wang, HEA-NiFeCuCoCe/NF through ultra-fast electrochemical self-reconstruction with high catalytic activity and corrosion resistance for seawater electrolysis, *Chem. Eng. J.*, 2023, **477**, 147286.

36 H. Guo, Z. Guo, K. Chu, W. Zong, H. Zhu, L. Zhang, C. Liu, T. Liu, J. Hofkens and F. Lai, Polymer-Confined Pyrolysis Promotes the Formation of Ultrafine Single-Phase High-Entropy Alloys: A Promising Electrocatalyst for Oxidation of Nitrogen, *Adv. Funct. Mater.*, 2023, **33**, 2308229.

37 C. Wang, J. Zhang, K. Miao, M. Long, S. Lai, S. Zhao and X. Kang, Octahedral Nanocrystals of Ru-Doped PtFeNiCuW/CNTs High-Entropy Alloy: High Performance Toward pH-Universal Hydrogen Evolution Reaction, *Adv. Mater.*, 2024, **36**, 2400433.

38 S. Wang, H. Yan, W. Huo, A. Davydok, M. Zając, J. Stępień, H. Feng, Z. Xie, J. K. Shang, P. H. C. Camargo, J. Jiang and F. Fang, Engineering multiple nano-twinned high entropy alloy electrocatalysts toward efficient water electrolysis, *Appl. Catal., B*, 2025, **363**, 124791.

39 P. Li, X. Wan, J. Su, W. Liu, Y. Guo, H. Yin and D. Wang, A Single-Phase FeCoNiMnMo High-Entropy Alloy Oxygen Evolution Anode Working in Alkaline Solution for over 1000 h, *ACS Catal.*, 2022, **12**, 11667–11674.